Co-located Observations of the E and F-region Thermosphere during a Substorm

D. D. Billett[1], K. A. McWilliams[1], M. G. Conde[2]

[1]Institute of Space and Atmospheric Studies, University of Saskatchewan, Saskatoon, SK, Canada
[2]Geophysical Institute, University of Alaska Fairbanks, Fairbanks, AK, USA

Key Points:

- Ionosphere-thermosphere coupling is examined at E- and F-region altitudes during a substorm, post-midnight above Poker Flat, Alaska
- E-region neutral winds are found to react slower to changes in the ionsophere due to substorm phases, compared to the F-region
- F-region heating is observed, and associated with neutral wind acceleration during substorm growth and recovery

Corresponding author: D. D. Billett, daniel.billett@usask.ca

Abstract

2D thermospheric wind fields, at both E- and F-region altitudes within a common vertical volume, were made using a Scanning Doppler Imager (SDI) at Poker Flat, Alaska, during a substorm event. Coinciding with these observations were F-region plasma velocity measurements from the Super Dual Auroral Radar Network (SuperDARN), and estimations of the total downward and upward field-aligned current density from the Active Magnetosphere and Planetary Electrodynamics Response Experiment (AMPERE). This combination of instruments gives an excellent opportunity to examine the spatial characteristics of high latitude ionosphere-thermosphere coupling, and how a process which is triggered in the magnetosphere (the substorm) affects that coupling at different altitudes. We find that during the substorm growth phase, the F-region thermospheric winds respond readily to an expanding ionospheric plasma convection pattern, whilst the E-region winds appear to take a much longer period of time. The differing response timescales of the E- and F-region winds is likely due to differences in neutral density at those altitudes, resulting in E-region neutrals being much more 'sluggish' with regards to ion-drag. We also observe increases in the F-region neutral temperature, associated with neutral winds accelerating during both substorm growth and recovery phases.

Plain Language Summary

At different altitudes in the polar atmosphere, how charged particles (the ionosphere) interact with neutral particles (the thermosphere) is of great importance. Primarily because collisions between the two is the mechanism by which energy from the solar wind is ultimately deposited into the atmosphere, from the magnetosphere. Magnetosphere-thermosphere energy exchange drives auroral displays, as well as contributes to heating in both the E-region (altitudes between 100-130 km) and F-region (altitudes between 150-300 km). The neutral atmosphere is significantly denser in the E-region compared to the F-region, so its interaction with the ionosphere at those different altitudes is quite different. In this study, we examined the E and F region during a "substorm" event, which is a large, sudden injection of energy into the nightside ionosphere. We found that the velocity of neutrals in the E-region reacted much more slowly than those in the F region, so that the conditions imposed on the E region before the substorm persisted during the substorm.

1 Introduction

Convection of plasma, embedded within the neutral thermosphere of Earth, dominates atmospheric flows at high altitudes and latitudes. Plasma convection is the result of the ionosphere being connected and disconnected from the interplanetary magnetic field (IMF) at the dayside and nightside magnetopause and magnetotail, increasing and decreasing total ionospheric flux, respectively (Cowley & Lockwood, 1992). Above around 150 km altitude, both ions and electrons move in the same direction so that the plasma has a bulk drift velocity perpendicular to the electric (**E**) and magnetic (**B**) fields, often creating a typical two-cell pattern of anti-sunward polar cap flow and sunward dawn/dusk flows. The orientation of the IMF plays a roll in the convection pattern morphology. In Geocentric Magnetic Coordinates (GSM), the IMF B_y component for instance controls where in local time magnetopause reconnection takes place, tilting the ionospheric convection pattern towards dawn or dusk accordingly (Heppner & Maynard, 1987; Ruohoniemi & Greenwald, 1996). Collisions between thermospheric neutrals and convecting ions (neglecting electrons as they are much less massive) can cause thermospheric neutrals at ionospheric altitudes to gain a large velocity component in the $\mathbf{E}\times\mathbf{B}$ direction through ion-drag. Thus, features of the ionospheric convection pattern are often visible in patterns of neutral winds, for instance, dawn and dusk plasma convection cells and an IMF B_y asymmetry (e.g. Richmond et al., 2003; Förster et al., 2008; Liu et al., 2020). A plasma convection dusk cell is more easily imprinted on the neutral flow than the dawn cell, due to reinforcement from the Coriolis force in the same direction in the dusk cell region.

A change from northward to southward directed IMF would begin to drive a two cell plasma convection pattern over the entire polar cap ionosphere within a relatively short timeframe, on the order of tens of minutes (Murr & Hughes, 2001). The "responsiveness" of the thermosphere to ionospheric changes depends on many factors. For instance, both plasma and neutral densities vary with local time and altitude. Thus, the ion-neutral collision frequency (i.e., the rate at which a given neutral particle collides with ions) also varies dependent on those factors. At auroral latitudes and latitudes, particle precipitation can also enhance collisions due to an increased plasma conductivity, resulting in thermospheric winds that align very quickly with the flow of plasma on the order of minutes (e.g. Billett et al., 2020; Conde et al., 2018; Kiene et al., 2018; Zou et al., 2018). During 'quiet' periods, i.e, times when the ionospheric conductivity is minimal or plasma convection velocity is slow, localised (mesoscale) neutral wind reconfig-

uration timescales are on the order of tens of minutes to hours at F-region altitudes (∼150-300 km; Cai et al., 2019; Xu et al., 2019, and references therein). In the lower E-region, the ion drift is impeded by neutral collisions, and can no longer be considered as $\mathbf{E} \times \mathbf{B}$ drifting (Sangalli et al., 2009). Plasma convection therefore takes much longer to accelerate the E-region neutrals that F-region neutrals, on the order of several hours (Richmond et al., 2003). These timescales are typically estimated from direct observations of the neutral and plasma velocities, and thus so far have been confined to limited regions, such as along satellite orbital paths (e.g. Killeen et al., 1984), or the fields-of-view of ground-based Fabry-Perot Interferometers (FPIs) (e.g, Billett et al., 2019) and radars (Kosch et al., 2001). An e-folding time, or thermospheric 'time constant', exists as a quantitative way of determining neutral wind reconfiguration timescales, which is defined as the time required for the neutral velocity to reach $1/e$ the speed of the plasma after a step change in the velocity difference between the two. However, changes to neutral flow because of ion-drag are often apparent sooner than the exact time constant. Other forces impose regular tides on thermospheric winds, in particular pressure forces from solar heating and the Coriolis effect. A consequence of a thermosphere that responds to ionospheric convection at varying rates is that the frictional energy exchange between plasma and neutral particles, or Joule heating, will be depend considerably on location, time and altitude.

Joule heating in the ionosphere is the largest sink of solar wind energy input at high-latitudes (Knipp et al., 2004). Typically poleward of 60° geomagnetic, electromagnetic field energy, carried as Poynting flux, is transferred from the magnetosphere to the ionosphere along geomagnetic field-aligned currents (FACs). The energy then dissipates in the ionosphere through Pedersen currents, parallel to the electric field, as Joule heating. Joule heating tends to be largest where the high-latitude convection electric field is also strong, i.e. near the sunward, low latitude return flow regions of convection at dawn and dusk (e.g., in empirical Joule heating models, such as Weimer, 2005). When taking into account the neutral wind, Joule heating can vary significantly in both rate of heating (Lu et al., 1995) and global morphology (Billett et al., 2018). Neutral temperatures also fluctuate expectedly in response, rising on the order of hundreds of Kelvin over periods of hours in both the E- and F-regions (Kurihara et al., 2006; Maeda et al., 2005; Price et al., 2019).

Substorms events, which are large inputs of energy to the atmosphere driven by episodes of magnetotail reconnection, are known to have a significant impact on ionospheric flows. Commonly, they are identified in the nightside auroral zone by observations of a sudden and spatially expansive increase in particle precipitation. There is commonly an enhancement of plasma convection equatorward during the substorm growth phase and then polarward during the substorm expansion phase (Lewis et al., 1998). The impact of substorms on the thermosphere is still under investigation, though it has been known for a while that they produce large changes to the thermospheric winds and neutral particle composition globally (e.g. Fujiwara et al., 1996, and references therin). Large increases in Joule heating due to the sudden injection of auroral energy trigger atmospheric gravity waves (AGWs) (Hines, 1960), which cause neutral wind disturbances to propagate to lower latitudes, and potentially even into the opposite hemisphere, as observed in simulations (Richmond & Matsushita, 1975; Fuller-Rowell et al., 1994). Other model simulations (e.g. Fuller-Rowell & Rees, 1984, and numerous since) found that ion drag was enhanced throughout the entire polar region during an isolated substorm, and Cai et al. (2019) noted similar strengthening of ion drag during substorm expansion on the mesoscale, using ground-based FPI observations. So far however, observations of the effect of substorms on neutral dynamics at both E- and F-region altitudes, with regards to ion-drag from plasma convection, have not been examined.

In this paper, we present sequential E- and F-region neutral wind measurements from a Scanning Doppler Imager (SDI) in Poker Flat, Alaska (Conde & Smith, 1995), which scanned post-midnight on October 14th, 2013. Observations coincided with a substorm event, which was identified using the auroral upper (AU) and lower (AL) indices from the OMNI dataset (`https://omniweb.gsfc.nasa.gov/`), along with FAC morphology changes by the Active Magnetosphere and Planetary Electrodynamics Response Experiment (AMPERE; Anderson et al., 2014). F-region neutral winds exhibited two prominent periods of equatorward acceleration coinciding with substorm growth and recovery, whilst the E-region winds appeared to be more tied to the $\mathbf{E} \times \mathbf{B}$ plasma convection velocities measured by the Super Dual Auroral Radar Network (SuperDARN; Greenwald et al., 1995). Neutral temperatures in the F region (also measured by the SDI) increased at times corresponding very closely to the equatorward neutral wind accelerations, consistent with an increase in the F-region Joule heating rate.

2 Intrumentation

2.1 The Scanning Doppler Imager

Situated in Poker Flat, Alaska, is a type of Fabry-Perot Interferometer (FPI) known as a Scanning Doppler Imager (SDI). This particular SDI (Conde & Smith, 1995, 1997) was developed and is currently operated by the University of Alaska Fairbanks' Geophysical Institute. The SDI measures optical emission spectra from the night sky, and by imaging both green (557.7 nm) and red (630 nm) line auroral emissions (corresponding to altitudes of approximately 100-130 km and 200-250 km, respectively), both E- and F-region neutral winds and temperatures can be obtained. A line-of-sight (LOS) Doppler spectrum is measured within a number of software defined regions known as 'zones'. The Doppler shift, spectral width (which gives the neutral temperature) and emission intensity are then calculated in each using a numerical fit (Conde, 2001). An assumption is made that the vertical wind across the field-of-view (FOV) of the SDI is homogeneous. The LOS velocity measured at the centre of the SDI (i.e., vertically along the zenith) can be considered entirely vertical wind, and the appropriate line-of-sight component of this wind is subtracted from all other LOS velocities to obtain an estimate for the complete horizontal wind vector field (Conde & Smith, 1998).

For the purposes of this study, the red line (630 nm) neutral winds have been mapped to an F-region altitude of 250 km (resulting in a FOV diameter of ∼1100 km), and the green line (557.7 nm) winds to an E-region altitude of 130 km (FOV diameter of ∼500 km). It should be noted that both the green and red line optical emission measurements are integrations over their respective altitude ranges. This is particularly problematic for the green line SDI measured temperatures, as auroral precipitating electrons with a higher characteristic energy cause the 557.7 nm emission layer to move to lower altitudes, where a higher neutral temperature is measured (Kaeppler et al., 2015). Any changes in the E-region neutral temperatures observed by the SDI are thus more indicative of green line emission layer height variability, than actual changes in temperature at a particular altitude. Measured F-region neutral temperatures are unaffected by this.

The time resolution of the SDI is slightly longer than 3 minutes for single wavelength exposures (630 nm or 557.7 nm), and the SDI alternates between the two wavelengths for the data shown in this study. A 115 zone configuration was used, allowing

for an average spatial resolution of around 70 km and 35 km in the F and E regions, respectively.

2.2 SuperDARN

The Super Dual Auroral Radar Network (SuperDARN) is a network of more than 30 high frequency radars located in both the northern and southern hemispheres, which measure the convection velocity of F-region ionospheric plasma (Chisham et al., 2007; Nishitani et al., 2019). Measurements from multiple radars can be combined onto a global scale grid, and a spherical harmonic fit to the data results in a global-scale estimation of the instantaneous pattern of electrostatic potential (Ruohoniemi & Greenwald, 1996). From the large scale maps of electrostatic potential, the horizontal plasma convection velocity ($\mathbf{v}$) can be calculated at any geographic position by assuming frozen-in plasma drift, where:

$$\mathbf{v} = \frac{-\nabla\Phi \times \mathbf{B}}{B^2} \tag{1}$$

$\nabla\Phi$ is the gradient of the electrostatic potential, equivalently the convection electric field, $\mathbf{E}$. The magnetic field, $\mathbf{B}$ is typically specified using the International Geomagnetic Reference Field (Thébault et al., 2015). The SuperDARN maps are constrained by *a priori* statistical convection model based on the IMF orientation (Thomas & Shepherd, 2018), which supplements regions where SuperDARN data coverage is low using the technique described by Ruohoniemi and Greenwald (1996). During the event presented in this study, SuperDARN data coverage was excellent in the region of interest (denoted later on by black dots in Figures 5 and 6.

The assumption of $\mathbf{E}\times\mathbf{B}$ drifting plasma is valid only within the F region, where the neutral density is low enough not to deviate ion flow substantially. E-region ionospheric scatter is discarded when creating SuperDARN convection maps by imposing a blanket slant range threshold on individual radar echos, typically by only using data recorded more than >800 km from the radar (Chisham & Pinnock, 2002). Although the measured F-region plasma velocity will not be totally representative of E-region plasma flows, it will however give an indication of the ion-drag force being hindered by the denser neutral atmosphere at E-region altitudes. SuperDARN convection map integration times are typically (and are in this paper) 2 minutes long.

2.3 AMPERE

The Active Magnetosphere and Planetary Electrodynamics Response Experiment (AMPERE) (Anderson et al., 2014) utilises magnetic field perturbation data from the Iridium communications satellite constellation to estimate the large scale magnitude and morphology of geomagnetic FACs. A spherical harmonic fit is applied to the magnetic perturbations, along with Ampere's law while assuming a vertical magnetic field. The resolution of AMPERE derived FACs are nominally 10 minutes temporally, and 1 hour (15 degrees) of magnetic local time spatially. An overview of the AMPERE mission and its scientific achievements is given by Coxon et al. (2018).

3 Observations

3.1 Neutral Winds

Figures 1 and 2 show consecutive neutral wind fields in the F-region (red line emission) and E-region (green line emission) thermosphere, respectively, measured by the Poker Flat SDI on the 14th October, 2013 between approximately 13 and 15 UT. Auroral emissions from around 12:30 UT onwards were bright, but it was cloudy above Poker Flat until 12:55 UT. Data measured by the SDI before that time is potentially unreliable, as cloud cover has the effect of removing angular information in the observed wind fields, so only integrations from 12:57 UT onwards are considered. Panels and vectors are orientated such that that the observer is looking down on the FOV from above, with geomagnetic north at the top and east to the right. Note that the colour scale, which represents the magnitude of the wind vectors (darker colours being faster speeds), is different in Figures 1 and 2, owing to the fact that the wind velocities are slower in the E-region. Meridional (north-south) and zonal (east-west) averages over the entire SDI FOV for both emissions are shown in Figure 3. The dashed lines in Figure 3 denote times shown later on, in Figures 5 and 6, for reference.

The F-region winds in Figures 1 and 3 (red lines) had velocity magnitudes that varied between 50 and 350 $\mathrm{m\,s^{-1}}$ and flowed mainly southward (equatorward), which is denoted by negative velocities. There are two distinct periods when the F-region winds across the entire FOV accelerated in the equatorward direction: from 12:57-13:19 UT (on average increasing from -135 to -195 $\mathrm{m\,s^{-1}}$) and from 13:49-14:27 UT (-80 to -230 $\mathrm{m\,s^{-1}}$). The two acceleration periods were separated by a period of slowing in between. Winds

observed in the most northern (poleward) zones of Figure 1 were the first to begin accelerating, and they were the last to slow down. From around 13:43 UT onwards, a westward turning of the wind, which also originated on the northern FOV, becomes more prominent. Winds on the southward edge of the FOV remained mainly equatorward for the entire period. The average zonal velocity was westward and fairly stable from around 14:30 UT onwards.

The E-region winds (Figures 2 and 3, green lines) were nearly always slower than the F-region winds. During the periods of equatorward acceleration seen clearly in the F-region data, the E-region winds also gained equatorward momentum. However, the E-region accelerations were not as large — from -35 to -85 $\mathrm{m\,s^{-1}}$ on average during the first period, and -35 to -60 $\mathrm{m\,s^{-1}}$ during the second. The 'recovery' of the E-region neutrals to a slower equatorward velocity (between 13:38 and 13:51 UT) also occurred later than in the F-region, which began recovering near instantly after the acceleration period. In contrast to the F-region wind morphology, the fastest E-region neutrals were on the south-eastern, and then, later, on the eastern side of the FOV. The eastern FOV was also the region where a significant portion of the E-region winds flowed eastward, as opposed to the mainly equatorward flowing F-region winds. Between 13:45-14:03 UT and from 14:40 UT onwards, there was a curvature of the E-region wind fields towards the east from the north.

3.2 Substorm and Convection Context

Figure 4 displays FAC measurements from AMPERE (top panel) along with geomagnetic AU and AL indices (bottom panel). The FAC data are presented in a keogram style, that is to say, a north-south slice taken through the centre of the SDI between 50 and 80 degrees geomagnetic latitude. Blue signifies the downward FAC (region 1, R1), while red is the upward FAC (region 2, R2) (Iijima & Potemra, 1976). Also highlighted are the periods of equatorward neutral wind acceleration, which are the same as those presented in Figure 3.

The period in Figure 4 labelled as the substorm growth phase (∼12:15 to 13:10 UT) is characterised by a gradual increase of the AU index and an equatorward movement of the R1 and R2 FAC bands. This interval also coincides reasonably well with the first equatorward acceleration period of the neutral wind. At ∼13:10 UT, a sharp decrease

of the AL index from -300 nT to -1000 nT, and the AU index continuing to rise to a peak of $\sim 250\,nT$, signals the substorm expansion phase. About 20 minutes after substorm expansion began, the R1 and R2 FAC bands started to contract poleward, which occurred while the the F-region neutral winds lost much of their equatorward momentum (in between the two shaded regions, Figure 3a). The gradual decrease in both AU and AL magnitude from 13:45 UT onwards is consistent with substorm recovery, however the FACs continued to contract before stabilising at 14:40 UT. The second period of equatorward acceleration of the neutral wind started almost as soon as AU began to decrease, and coincided with a strong intensification of the FAC density.

Figures 5 and 6 show snapshots of the high-latitude plasma convection pattern, measured by the SuperDARN, with corresponding SDI neutral wind fields for the F and E regions, respectively. The times shown are those labelled in Figure 3. The plots are in a geomagnetic polar format, with magnetic midnight to the bottom and dawn to the right, fixed on the location of the SDI at Poker Flat, Alaska. The E-region panels are more "zoomed in" due to the lower altitude projection, and black dots show where SuperDARN radars obtained ionospheric backscatter. In order to interpret whether ion drag was influential on both the F- and E-region neutral winds, the prevailing plasma convection conditions need to be examined closely. However, because ion-drag is not instantly apparent in neutral wind velocities, panels shown in Figures 5 and 6 represent conditions before (t_a , t_d), during (t_b , t_e), and after (t_c , t_f) the first (t_{a-c}) and second (t_{d-f}) acceleration periods (12:57-13:19 UT and 13:49-14:27 UT), respectively. This translates to magnetic local times roughly between 02 and 04, placing the SDI FOV consistently within the dawnside convection return flow region.

Between panels t_a, t_b and t_c in Figures 5 and 6, the plasma convection pattern expanded equatorward. The plasma convection also had an equatorward directed electric field (directed perpendicular to the plasma $\mathbf{E}\times\mathbf{B}$ flow contours, which were eastward). The F-region neutral winds thus mainly flowed, and accelerated, in the direction of the electric field (outwards from the centre of the convection cell) during the first acceleration period. The electric field magnitude however (represented by the density of electrostatic potential contours) did not increase significantly until after the first acceleration period (panel t_c). Moreover, in Figure 6t_b, the E-region neutral winds accelerated only partly in the electric field direction (equatorward), after initially being closer to the $\mathbf{E}\times\mathbf{B}$ direction in panel t_a. The slight acceleration of the E-region winds in the elec-

tric field direction is more easily seen as the meridional acceleration of the green line between times t_a and t_b in Figure 3a. Between t_c and t_d of Figure 5, the F-region winds slowed in the electric field direction and there was not much change to to the morphology of the dawnside plasma convection cell. However, the maximum electrostatic potential of the dawn cell (at the cell foci) was higher than at the beginning of the event (27 kV versus 15 kV).

During the second acceleration period (see t_e in Figures 5 and 6), the IMF B_y component turned from positive to negative and the dawn convection cell tilted clockwise. The maximum dawnside electrostatic potential value had also increased again, to 33 kV. The F-region winds sped up considerably in the equatorward electric field direction, but the E-region winds became more aligned into the $\mathbf{E}\times\mathbf{B}$ direction (Figure 6t_e and t_f). The alignment of the E-region winds with eastward plasma convection can also be seen in Figure 3, as their zonal velocity (panel b, green line) increases slightly in the eastward direction after t_d. Similar neutral wind and plasma convection conditions persisted until after the second acceleration period (Figures 5 and 6, t_f); the F-region neutral wind was mainly $\mathbf{E}$ field aligned, whilst the E-region wind $\mathbf{E}\times\mathbf{B}$ aligned.

3.3 Neutral Temperatures

Average neutral temperatures above Poker Flat, also measured by the SDI, are shown in Figure 7 for both the F (panel a) and E regions (panel b). This is the same time period shown in Figure 3, so the first ∼20 minutes of observations were cloudy. However, unlike neutral winds recorded by the SDI, neutral temperature averages are fairly unaffected by cloud unless the emission brightness is very low. It's important to recall, as mentioned prior, that the E-region temperatures measured by the SDI are more sensitive to the height variability of the 557.7 nm emission, rather than in situ temperature changes at a specific altitude. For continuity of language within this section, we refer to the 557.7 nm green line emission temperatures as "E-region temperatures", even though they vary significantly in altitude within the E-region range. We discuss further the meaning of E-region temperature changes with regards to altitude later on in the discussion section.

On average, F-region temperatures (Figure 7a) rose during two distinct periods: 13:03-13:34 UT and 13:58-14:26 UT, both of which were almost concurrent with the two

equatorward neutral wind acceleration periods. The periods of F-region temperature increase lagged the neutral wind acceleration by around 5 minutes for the first period, and by around 10 minutes for the second period. Those were average increases from 830-915 K and 912-995 K, respectively.

The average temperature in the E region rose from 320-445 K between 13:02 and 13:38 UT (Figure 7b). Similar to the initial temperature increase in the F-region (Figure 7a), this temperature increase coincided reasonably well with the first equatorward acceleration period and substorm growth, but continued for approximately 20 minutes after the end of the acceleration period. The rate of temperature increase after the first acceleration period appeared to slow down until it reached its peak value of 445 K at 13:38 UT. Between 13:38 and 13:51 UT, there was a sharp drop in E-region temperature to 315 K, which coincided with the substorm recovery phase. There was no significant increase of the E-region temperature during the second neutral wind acceleration period, apart from small rises within one standard deviation. The E-region temperature gradually decreased for the remainder of the event.

4 Discussion

The event presented in this study displays large and distinct periods of equatorward acceleration in the F-region neutral winds. This was initially was thought to be unusual because the observations were made just post-midnight in magnetic local time, around late autumn/early wintertime, when gradients in solar heating would be fairly small and would not contribute to the acceleration that was seen (Dhadly et al., 2018). There was also a period in between the two acceleration intervals where the neutral wind slowed, indicating an external equatorward force becoming subsequently stronger, weaker, then stronger again. After examination of the FACs from AMPERE, along with the AU and AL indices, it was found that the acceleration periods coincided with substorm phases. We believe the substorm influenced the neutral winds via ion-drag, specifically, the expansion and contraction of the plasma convection pattern. The large differences between behaviours of the E- and F-region winds can be explained by the different timescales that those two regions respond to ion-drag changes. The F-region neutral temperature increases, coinciding with the wind accelerations, can be attributed to Joule heating. Finally, the E-region temperature variations are indicative of changes to the characteristic energy of

359 precipitating electrons in the lower thermosphere caused by a change in the 557.7 nm emis-
360 sion altitude (Kaeppler et al., 2015).

361 Substorm growth is characterised by the gradual strengthening of plasma convec-
362 tion and therefore of the electrojet currents. Substorm growth is identified by an increase
363 in magnitude of both the AU and AL indices, such as those in Figure 4, which respond
364 to intensification of the eastward and westward auroral electrojet currents. The polar
365 cap also expands during the growth phase, as the R1/R2 currents measured by AMPERE
366 and the equatorward edge of the plasma convection pattern measured by SuperDARN
367 (Figures 5 and 6, t_a and t_b) move equatorward. The FAC and plasma convection expan-
368 sion are consistent with an increase in polar cap flux due to dayside reconnection, and
369 both are well known signatures of the substorm growth phase (e.g. Lewis et al., 1997;
370 Milan et al., 2003; Coxon et al., 2014). In the reference frame of the neutral gas above
371 Poker Flat, ion-drag would act in two directions, on two different timescales. On a long
372 timescale encompassing the entire duration of the event, the sunward $\mathbf{E}\times\mathbf{B}$ drifting plasma
373 persistently applies ion-drag in the eastward direction. There is also an ion-drag force
374 that acts in the equatorward direction over a short timescale, associated with southward
375 ion motion due to the expanding convection pattern, for an interval on the order of tens
376 of minutes.

377 The first equatorward neutral wind acceleration period coincided with an equator-
378 ward expansion of the plasma convection pattern, between 12:57 and 13:19 UT. Exam-
379 ining the neutral winds in context with the SuperDARN electrostatic potential contours
380 (shown in Figures 5 and 6) reveals that this acceleration was in the electric field direc-
381 tion (panels t_{a-c}), i.e., the direction of expanding convection and corresponding equa-
382 torward ion drag. Although the E-region winds experienced this acceleration (see the
383 average meridional velocities, Figure 3a), it was to a much lesser degree. E-region winds
384 consistently had velocity component in the $\mathbf{E}\times\mathbf{B}$ direction (eastward, positive zonal),
385 implying competing ion-drag forcing from both the long timescale $\mathbf{E}\times\mathbf{B}$ drifting plasma
386 and the short timescale equatorward expanding convection boundary.

387 During the event, ion-drag forcing in the $\mathbf{E}\times\mathbf{B}$ direction was constantly imposed
388 on the neutrals at both E- and F-region altitudes, over several hours, in the eastward
389 direction. Comparatively, the ion-drag force acting equatorward during substorm growth
390 phase acted for approximately 30 minutes. From previous studies, timescales needed for

the thermosphere to fully re-orientate due to ion-drag are on the order of tens of minutes for the F-region, and hours for the E-region (Kosch et al., 2001; Richmond et al., 2003). The E-region neutrals not turning fully equatorward could be because ion-drag was simply not acting for a long enough period of time in that direction, but it was more than long enough for the F-region neutrals to do so. The F-region winds also decelerated more quickly than those in the E-region after the plasma convection expansion stopped, indicating again that F-region neutral winds were responding to ion-drag on shorter timescales. Additionally, the E-region winds were far less variable, probably because the neutrals at that altitude are much denser than in the F-region. Because the polar neutral winds in the E-region take so long to respond to ion-drag changes, they inherently had embedded within them the last few hours of previous plasma convection conditions, i.e. a persistently eastward flow component. The F-region winds on the other hand reflect plasma convection conditions on short timescales (tens of minutes to an hour), resulting in their equatorward acceleration during the ∼30 minute long substorm growth phase.

Substorm expansion onset occurred when the AL index sharply decreased at ∼13:10 UT (Figure 4), indicating an enhancement of the substorm electrojet and the sudden onset of magnetotail reconnection (Kepko et al., 2015). The R1 and R2 FACs measured by AMPERE began to contract poleward within about 20 minutes. The FACs also intensified, implying the removal of nightside flux and also consistent with previous FAC onset observations (e.g. Clausen et al., 2013; Coxon et al., 2014). After onset, and during the first part of poleward motion of the FACs, was when both the E and F-region neutral winds slowed meridionally (Figure 3a), consistent with ion-drag continuing to act primarily in the $\mathbf{E}\times\mathbf{B}$ direction but no longer in the equatorward direction (Figures 5 and 6, t_c and t_d). As the SDI co-rotated with Earth towards the dayside (13:00 UT onwards), there was a gradual increase of the F-region westward velocity (Figure 3b). This is probably a response to the pressure gradient caused by gradually increasing solar heating, which at dawn, would be directed westward (i.e. anti-sunward), and is common of F-region winds post-midnight (Dhadly et al., 2017). The E-region winds retaining an eastward component (aligned with $\mathbf{E} \times \mathbf{B}$ drifting plasma) could in part be due to the long E-region ion-drag timescales discussed earlier, but also reflect that the ion-neutral collision frequency at lower altitudes is much higher when compared to F-region altitudes. Thus E-region winds better represent the strengthening westward electrojet current during substorm expansion, in agreement with Cai et al. (2019).

The second equatorward acceleration of the neutral winds occurred during substorm recovery, following soon after the intensification of FACs during substorm expansion. This implies strong auroral activity in the vicinity of the SDI (dashed line in Figure 4, top panel), and would result in increased Joule and auroral heating. Indeed, inspection of images from the Poker Flat all-sky camera (not shown, but can be accessed along with the SDI data link supplied in the acknowledgements) showed that bright auroral displays coincided with the intensification of upward FAC (downward precipitating electrons), shown in Figure 4. The dawnside ionospheric electric field/electric potential gradient is also increased from this time onwards (Figures 5 and 6, panels d, e and f), which would contribute further to Joule heating. These are known sources of enhanced neutral winds (Deng et al., 2008; Tsuda et al., 2009; Wang et al., 2017; Cai et al., 2019), and are likely the biggest contributors to the second equatorward neutral wind acceleration rather than ion-drag.

There is clear evidence of F-region Joule heating during the event. Joule heating of neutrals occurs very soon during the two periods of neutral wind acceleration in Figure 7a, with the temperature stabilising after the neutrals begin to slow. This heating is consistent with increased friction between the neutrals and plasma leading to Joule heating (Billett et al., 2018). Part of the neutral temperature increase, however, will be from auroral heating brought about by the substorm and resulting electron precipitation (Hays et al., 1973). Although, the majority of auroral particle heating during substorms is likely to be deposited at lower, E-region altitudes (Vickrey et al., 1982). It appears that for this event, Joule heating is the dominant source of the neutral heating in the F-region due to coincidence with the neutral wind acceleration. It is interesting to see Joule heating as a significant driver of neutral temperatures in the F-region, particularly because Pedersen currents (which Joule heating dissipates through) do not typically have a large magnitude in the F-region compared to the E-region.

It has known for a while that the neutral temperatures measured by SDIs using green line (557.7 nm) emissions were more indicative of changes in the green line emission altitude, rather than in situ temperature changes at a certain altitude (Hecht et al., 2006, and references therin). Kaeppler et al. (2015), using the same SDI as the one used in this study, examined the relationship between green line neutral temperature measurements and the characteristic energy of the precipitating electrons involved. Along with verification data from the Poker Flat Incoherent Scatter Radar (PFISR), it was shown

that increases to the SDI measured 557.7 nm neutral temperatures corresponded to a decreased ('softened') auroral characteristic energy, and increased 557.7 nm emission altitude. Applying the results from Kaeppler et al. (2015) for a strong (>1 kR) green line emission event, to the E-region neutral temperature changes presented in section 3.3, the temperature increase from 320-445 K between 13:02 and 13:38 UT corresponds to an auroral electron characteristic energy decrease, or softening, from ∼1.5 to ∼1 keV. This energy change translates to the peak green line emission altitude increasing only by about 5 km, from approximately 115 to 120 km, starting at substorm growth phase until approximately 20 minutes after the onset of expansion. The later temperature drop to 315 K, which took place over a much shorter period of time than the more gradual increase earlier on, implies a quick hardening of precipitation to higher energies as the electrons penetrate to deeper altitudes. And indeed, the sharp temperature drop coincides well with the intensification of upward FAC (downward electrons) in Figure 4.

5 Summary

We have presented co-located E- and F-region neutral winds and temperatures measured by a Scanning Doppler Imager above Poker Flat, Alaska, during a substorm. From these observations, we have seen that the E- and F-region thermosphere responds quite differently to the changing ion-drag conditions, as well as to increased Joule heating. In particular:

- F-region winds in the post-midnight magnetic local time sector respond quickly to an equatorward expanding plasma convection pattern during the substorm growth phase by accelerating equatorward. E-region winds respond in a similar way, but the magnitude of their acceleration is smaller and occurs over a longer period.
- Neutral winds in the E-region are slow to respond to the ion-drag force from the expanding plasma convection pattern, because the expansion itself occurs on timescales of the order of tens of minutes. This is not long enough to exceed the ion-neutral 'time constant' for the E-region, which is likely to be on the order of hours due to its higher neutral density and therefore higher viscosity.
- Because of their long ion-neutral coupling timescale, E-region winds throughout the entire substorm had embedded within them the average of several hours' worth of enhanced ion-drag forcing, including that which occurred before substorm on-

set. That is, the E-region winds were consistently directed in the prevailing $\mathbf{E}\times\mathbf{B}$ drifting plasma direction.

- Because of their shorter ion-neutral coupling timescale, F-region winds responded more quickly to changes in the plasma convection pattern associated with substorm growth, expansion and recovery. Thus, they had a more short-term (∼10s of minutes) variability.
- Heating of the F-region neutrals coincided with large velocity changes, consistent with increased F-region Joule heating during substorm growth and recovery due to ion-neutral friction.

Acknowledgments

This research was supported by the National Sciences and Engineering Research Council of Canada (NSERC). DDB was supported by NSERC CREATE Grant #479771-20, whilst KM was supported by NSERC Discovery Grant #RGPIN 05472-2017. The authors acknowledge the use of data from SuperDARN, an international project made possible by the national funding agencies of Australia, Canada, China, France, Japan, South Africa, the United Kingdom and the United States of America. SuperDARN data can be downloaded from Globus, instructions of which are provided here: `https://github.com/SuperDARNCanada/globus`. SuperDARN data in this study was processed using the Radar Software Toolkit (RST), version 4.3: `https://github.com/SuperDARN/rst`. The Poker Flat Scanning Doppler Imager was developed and is currently operated by the University of Alaska Fairbanks' Geophysical Institute, of which the data can be accessed from: `http://sdi_server.gi.alaska.edu/sdiweb/index.asp`. Development and operation of the SDI was supported by the US National Science Foundation award number 1140075. We also thank the AMPERE team and the AMPERE Science Center for providing the Iridium derived data products, which can be plotted and downloaded at: `http://ampere.jhuapl.edu/`.

References

Anderson, B. J., Korth, H., Waters, C. L., Green, D. L., Merkin, V. G., Barnes, R. J., & Dyrud, L. P. (2014). Development of large-scale birkeland currents determined from the active magnetosphere and planetary electrodynamics response experiment. *Geophysical Research Letters*, *41*(9), 3017–3025.

Billett, D. D., Grocott, A., Wild, J. A., Walach, M.-T., & Kosch, M. J. (2018). Diurnal variations in global Joule heating morphology and magnitude due to neutral winds. *Journal of Geophysical Research: Space Physics*, *123*(3), 2398–2411.

Billett, D. D., Hosokawa, K., Grocott, A., Wild, J. A., Aruliah, A. L., Ogawa, Y., ... Lester, M. (2020). Multi-instrument observations of ion-neutral coupling in the dayside cusp. *Geophysical Research Letters*, *47*(4), e2019GL085590. doi: 10.1029/2019GL085590

Billett, D. D., Wild, J. A., Grocott, A., Aruliah, A. L., Ronksley, A. M., Walach, M.-T., & Lester, M. (2019). Spatially resolved neutral wind response times during high geomagnetic activity above Svalbard. *Journal of Geophysical Research: Space Physics*, *124*(8), 6950-6960.

Cai, L., Oyama, S., Aikio, A., Vanhamäki, H., & Virtanen, I. (2019). Fabry-Perot interferometer observations of thermospheric horizontal winds during magnetospheric substorms. *Journal of Geophysical Research: Space Physics*, *124*(5), 3709–3728.

Chisham, G., Lester, M., Milan, S. E., Freeman, M. P., Bristow, W. A., Grocott, A., ... others (2007). A decade of the super dual auroral radar network (SuperDARN): Scientific achievements, new techniques and future directions. *Surveys in geophysics*, *28*(1), 33–109.

Chisham, G., & Pinnock, M. (2002). Assessing the contamination of superdarn global convection maps by non-f-region backscatter. *Annales Geophysicae*, *20*(1), 13–28.

Clausen, L. B. N., Milan, S. E., Baker, J. B. H., Ruohoniemi, J. M., Glassmeier, K.-H., Coxon, J. C., & Anderson, B. J. (2013). On the influence of open magnetic flux on substorm intensity: Ground-and space-based observations. *Journal of Geophysical Research: Space Physics*, *118*(6), 2958–2969.

Conde, M. (2001). Analysis of Fabry-Perot spectra of lidar backscatter echoes. *ANARE Reports*, *146*, 91–114.

Conde, M., Bristow, W. A., Hampton, D. L., & Elliott, J. (2018). Multiinstrument studies of thermospheric weather above Alaska. *Journal of Geophysical Research: Space Physics*, *123*(11), 9836–9861.

Conde, M., & Smith, R. W. (1995). Mapping thermospheric winds in the auroral

zone. *Geophysical research letters*, *22*(22), 3019–3022.

Conde, M., & Smith, R. W. (1997). Phase compensation of a separation scanned, all-sky imaging Fabry–Perot spectrometer for auroral studies. *Applied optics*, *36*(22), 5441–5450.

Conde, M., & Smith, R. W. (1998). Spatial structure in the thermospheric horizontal wind above Poker Flat, Alaska, during solar minimum. *Journal of Geophysical Research: Space Physics*, *103*(A5), 9449–9471.

Cowley, S. W. H., & Lockwood, M. (1992, Feb). Excitation and decay of solar wind-driven flows in the magnetosphere-ionosphere system. *Annales Geophysicae*, *10*(1-2), 103-115.

Coxon, J. C., Milan, S. E., & Anderson, B. J. (2018). A review of birkeland current research using AMPERE. *Electric currents in geospace and beyond*, 257–278.

Coxon, J. C., Milan, S. E., Clausen, L. B. N., Anderson, B. J., & Korth, H. (2014). A superposed epoch analysis of the regions 1 and 2 birkeland currents observed by AMPERE during substorms. *Journal of Geophysical Research: Space Physics*, *119*(12), 9834–9846.

Deng, Y., Richmond, A. D., Ridley, A. J., & Liu, H.-L. (2008). Assessment of the non-hydrostatic effect on the upper atmosphere using a general circulation model (gcm). *Geophysical Research Letters*, *35*(1).

Dhadly, M. S., Emmert, J., Drob, D., Conde, M., Doornbos, E., Shepherd, G., ... Ridley, A. (2017). Seasonal dependence of northern high-latitude upper thermospheric winds: A quiet time climatological study based on ground-based and space-based measurements. *Journal of Geophysical Research: Space Physics*, *122*(2), 2619–2644.

Dhadly, M. S., Emmert, J. T., Drob, D. P., Conde, M. G., Doornbos, E., Shepherd, G. G., ... Ridley, A. J. (2018). Seasonal dependence of geomagnetic active-time northern high-latitude upper thermospheric winds. *Journal of Geophysical Research: Space Physics*, *123*(1), 739–754.

Förster, M., Rentz, S., Köhler, W., Liu, H., & Haaland, S. E. (2008). IMF dependence of high-latitude thermospheric wind pattern derived from CHAMP cross-track measurements. *Annales Geophysicae*, *26*(6), 1581–1595.

Fujiwara, H., Maeda, S., Fukunishi, H., Fuller-Rowell, T. J., & Evans, D. S. (1996). Global variations of thermospheric winds and temperatures caused by sub-

storm energy injection. *Journal of Geophysical Research: Space Physics*, *101*(A1), 225–239.

Fuller-Rowell, T. J., Codrescu, M. V., Moffett, R. J., & Quegan, S. (1994). Response of the thermosphere and ionosphere to geomagnetic storms. *Journal of Geophysical Research: Space Physics*, *99*(A3), 3893–3914.

Fuller-Rowell, T. J., & Rees, D. (1984). Interpretation of an anticipated long-lived vortex in the lower thermosphere following simulation of an isolated substorm. *Planetary and space science*, *32*(1), 69–85.

Greenwald, R. A., Baker, K. B., Dudeney, J. R., Pinnock, M., Jones, T. B., Thomas, E. C., ... others (1995). Darn/superdarn. *Space Science Reviews*, *71*(1-4), 761–796.

Hays, P. B., Jones, R. A., & Rees, M. H. (1973). Auroral heating and the composition of the neutral atmosphere. *Planetary and Space Science*, *21*(4), 559–573.

Hecht, J. H., Strickland, D. J., & Conde, M. G. (2006). The application of ground-based optical techniques for inferring electron energy deposition and composition change during auroral precipitation events. *Journal of atmospheric and solar-terrestrial physics*, *68*(13), 1502–1519.

Heppner, J. P., & Maynard, N. C. (1987). Empirical high-latitude electric field models. *Journal of Geophysical Research: Space Physics*, *92*(A5), 4467–4489.

Hines, C. O. (1960). Internal atmospheric gravity waves at ionospheric heights. *Canadian Journal of Physics*, *38*(11), 1441–1481.

Iijima, T., & Potemra, T. A. (1976). Field-aligned currents in the dayside cusp observed by triad. *Journal of Geophysical Research*, *81*(34), 5971–5979.

Kaeppler, S. R., Hampton, D. L., Nicolls, M. J., Strømme, A., Solomon, S. C., Hecht, J. H., & Conde, M. G. (2015). An investigation comparing ground-based techniques that quantify auroral electron flux and conductance. *Journal of Geophysical Research: Space Physics*, *120*(10), 9038–9056.

Kepko, L., McPherron, R. L., Amm, O., Apatenkov, S., Baumjohann, W., Birn, J., ... Sergeev, V. (2015). Substorm current wedge revisited. *Space Science Reviews*, *190*(1-4), 1–46.

Kiene, A., Bristow, W. A., Conde, M. G., & Hampton, D. L. (2018). Measurements of ion-neutral coupling in the auroral F region in response to increases in particle precipitation. *Journal of Geophysical Research: Space Physics*, *123*(5),

3900–3918.

Killeen, T. L., Hays, P. B., Carignan, G. R., Heelis, R. A., Hanson, W. B., Spencer, N. W., & Brace, L. H. (1984). Ion-neutral coupling in the high-latitude F region: Evaluation of ion heating terms from Dynamics Explorer 2. *Journal of Geophysical Research: Space Physics*, *89*(A9), 7495-7508.

Knipp, D. J., Tobiska, W. K., & Emery, B. (2004). Direct and indirect thermospheric heating sources for solar cycles 21–23. *Solar Physics*, *224*(1-2), 495.

Kosch, M., Cierpka, K., Rietveld, M., Hagfors, T., & Schlegel, K. (2001). High-latitude ground-based observations of the thermospheric ion-drag time constant. *Geophysical research letters*, *28*(7), 1395–1398.

Kurihara, J., Abe, T., Oyama, K.-I., Griffin, E., Kosch, M., Aruliah, A., ... Iwagami, N. (2006). Observations of the lower thermospheric neutral temperature and density in the DELTA campaign. *Earth, planets and space*, *58*(9), 1123–1130.

Lewis, R. V., Freeman, M. P., & Reeves, G. D. (1998). The relationship of hf radar backscatter to the accumulation of open magnetic flux prior to substorm onset. *Journal of Geophysical Research: Space Physics*, *103*(A11), 26613–26619.

Lewis, R. V., Freeman, M. P., Rodger, A. S., Reeves, G. D., & Milling, D. K. (1997). The electric field response to the growth phase and expansion phase onset of a small isolated substorm. In *Annales geophysicae* (Vol. 15, pp. 289–299).

Liu, J., Burns, A. G., Wang, W., & Zhang, Y. (2020). Modelled imf by effects on the polar ionosphere and thermosphere coupling. *Journal of Geophysical Research: Space Physics*, e2019JA026949.

Lu, G., Richmond, A. D., Emery, B. A., & Roble, R. G. (1995). Magnetosphere-ionosphere-thermosphere coupling: Effect of neutral winds on energy transfer and field-aligned current. *Journal of Geophysical Research: Space Physics*, *100*(A10), 19643–19659.

Maeda, S., Nozawa, S., Ogawa, Y., & Fujiwara, H. (2005). Comparative study of the high-latitude e region ion and neutral temperatures in the polar cap and the auroral region derived from the EISCAT radar observations. *Journal of Geophysical Research: Space Physics*, *110*(A8).

Milan, S. E., Lester, M., Cowley, S. W. H., Oksavik, K., Brittnacher, M., Greenwald, R. A., ... Villain, J.-P. (2003). Variations in the polar cap area during two

substorm cycles. *Annales Geophysicae*, *21*(5), 1121-1140.

Murr, D. L., & Hughes, W. J. (2001). Reconfiguration timescales of ionospheric convection. *Geophysical Research Letters*, *28*(11), 2145-2148. doi: 10.1029/2000GL012765

Nishitani, N., Ruohoniemi, J. M., Lester, M., Baker, J. B. H., Koustov, A. V., Shepherd, S. G., ... others (2019). Review of the accomplishments of mid-latitude super dual auroral radar network (SuperDARN) HF radars. *Progress in Earth and Planetary Science*, *6*(1), 1–57.

Price, D. J., Whiter, D. K., Chadney, J. M., & Lanchester, B. S. (2019). High-resolution optical observations of neutral heating associated with the electrodynamics of an auroral arc. *Journal of Geophysical Research: Space Physics*, *124*(11), 9577–9591.

Richmond, A. D., Lathuillère, C., & Vennerstroem, S. (2003). Winds in the high-latitude lower thermosphere: Dependence on the interplanetary magnetic field. *Journal of Geophysical Research: Space Physics*, *108*(A2). doi: 10.1029/2002JA009493

Richmond, A. D., & Matsushita, S. (1975). Thermospheric response to a magnetic substorm. *Journal of Geophysical Research*, *80*(19), 2839–2850.

Ruohoniemi, J. M., & Greenwald, R. A. (1996). Statistical patterns of high-latitude convection obtained from goose bay hf radar observations. *Journal of Geophysical Research: Space Physics*, *101*(A10), 21743–21763.

Sangalli, L., Knudsen, D. J., Larsen, M. F., Zhan, T., Pfaff, R. F., & Rowland, D. (2009). Rocket-based measurements of ion velocity, neutral wind, and electric field in the collisional transition region of the auroral ionosphere. *Journal of Geophysical Research: Space Physics*, *114*(A4).

Thébault, E., Finlay, C. C., Beggan, C. D., Alken, P., Aubert, J., Barrois, O., ... others (2015). International geomagnetic reference field: the 12th generation. *Earth, Planets and Space*, *67*(1), 79.

Thomas, E. G., & Shepherd, S. G. (2018). Statistical patterns of ionospheric convection derived from mid-latitude, high-latitude, and polar superdarn hf radar observations. *Journal of Geophysical Research: Space Physics*, *123*(4), 3196–3216.

Tsuda, T. T., Nozawa, S., Oyama, S., Motoba, T., Ogawa, Y., Shinagawa, H., ...

others (2009). Acceleration mechanism of high-speed neutral wind observed in the polar lower thermosphere. *Journal of Geophysical Research: Space Physics*, *114*(A4).

Vickrey, J. F., Vondrak, R. R., & Matthews, S. J. (1982). Energy deposition by precipitating particles and joule dissipation in the auroral ionosphere. *Journal of Geophysical Research: Space Physics*, *87*(A7), 5184–5196.

Wang, H., Zhang, K. D., Wan, X., & Lühr, H. (2017). Universal time variation of high-latitude thermospheric disturbance wind in response to a substorm. *Journal of Geophysical Research: Space Physics*, *122*(4), 4638–4653.

Weimer, D. R. (2005). Improved ionospheric electrodynamic models and application to calculating Joule heating rates. *Journal of Geophysical Research: Space Physics*, *110*(A5).

Xu, H., Shiokawa, K., Oyama, S.-i., & Otsuka, Y. (2019). Thermospheric wind variations observed by a Fabry–Perot interferometer at tromsø, norway, at substorm onsets. *Earth, Planets and Space*, *71*(1), 93.

Zou, Y., Nishimura, Y., Lyons, L., Conde, M., Varney, R., Angelopoulos, V., & Mende, S. (2018). Mesoscale F region neutral winds associated with quasi-steady and transient nightside auroral forms. *Journal of Geophysical Research: Space Physics*, *123*(9), 7968–7984.

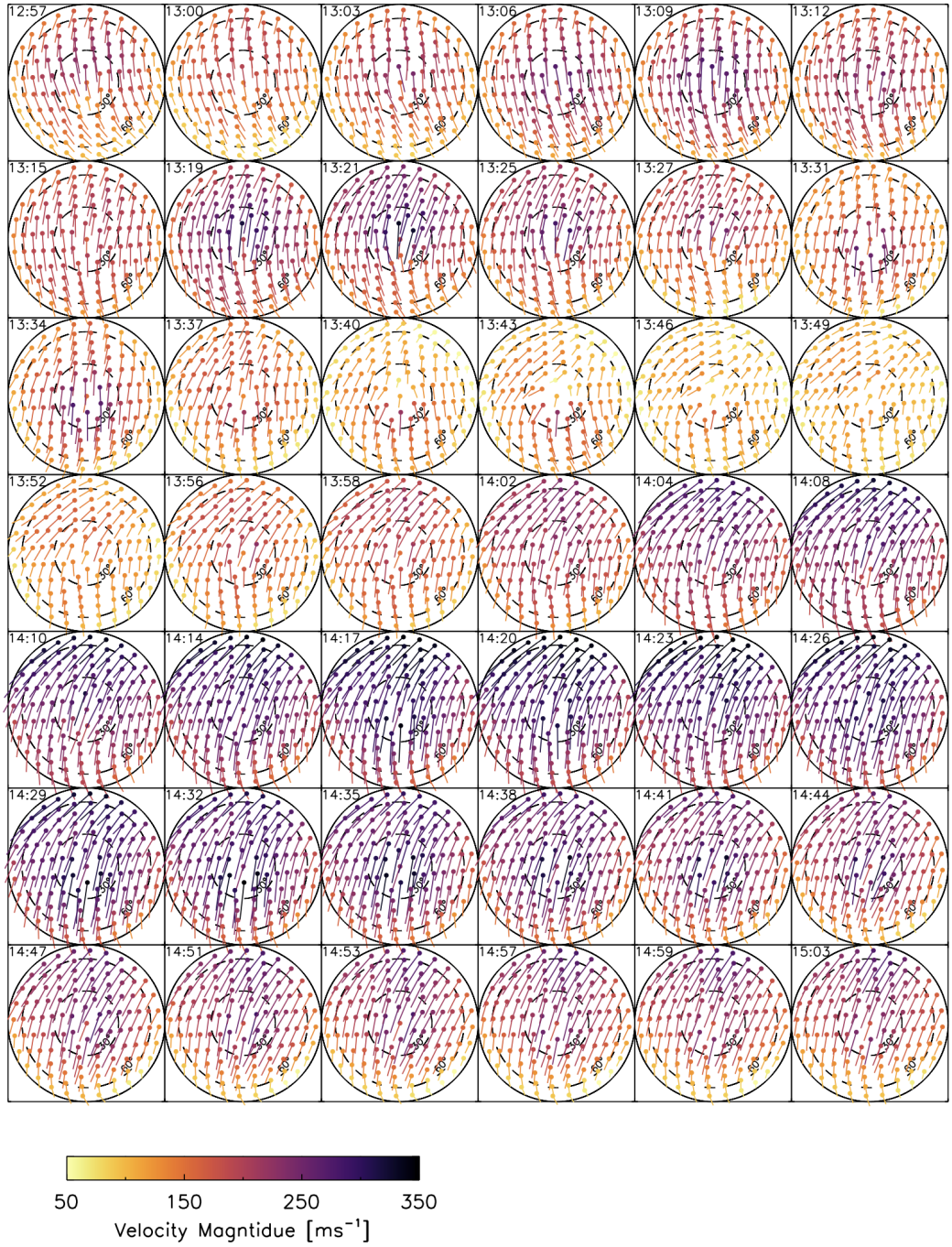

Figure 1. Consecutive red line (630 nm) neutral wind fields measured by the Poker Flat SDI on the 14th October, 2013, between 12:57 and 15:03 UT. Concentric circles are zenith angles from the centre of the FOV (0° zenith), spaced by 30° up to a maximum of 73°. Velocity vectors are coloured according to their magnitude, given in the colour bar. Panels and vectors are orientated with geomagnetic north as up, and geomagnetic east to the right. The base of the vectors are given by dots.

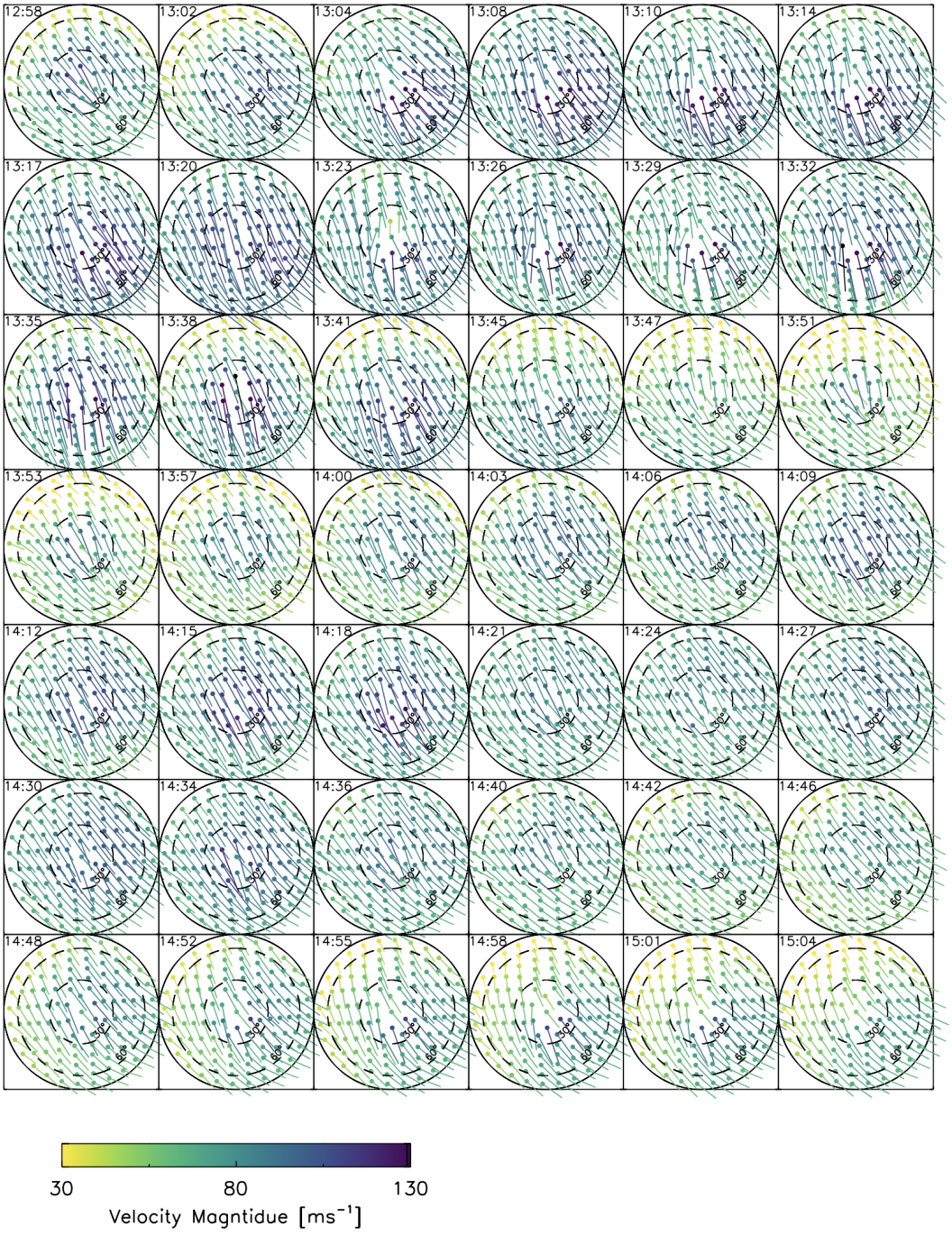

Figure 2. Same as Figure 1, but for the green line (557.7 nm) neutral wind fields.

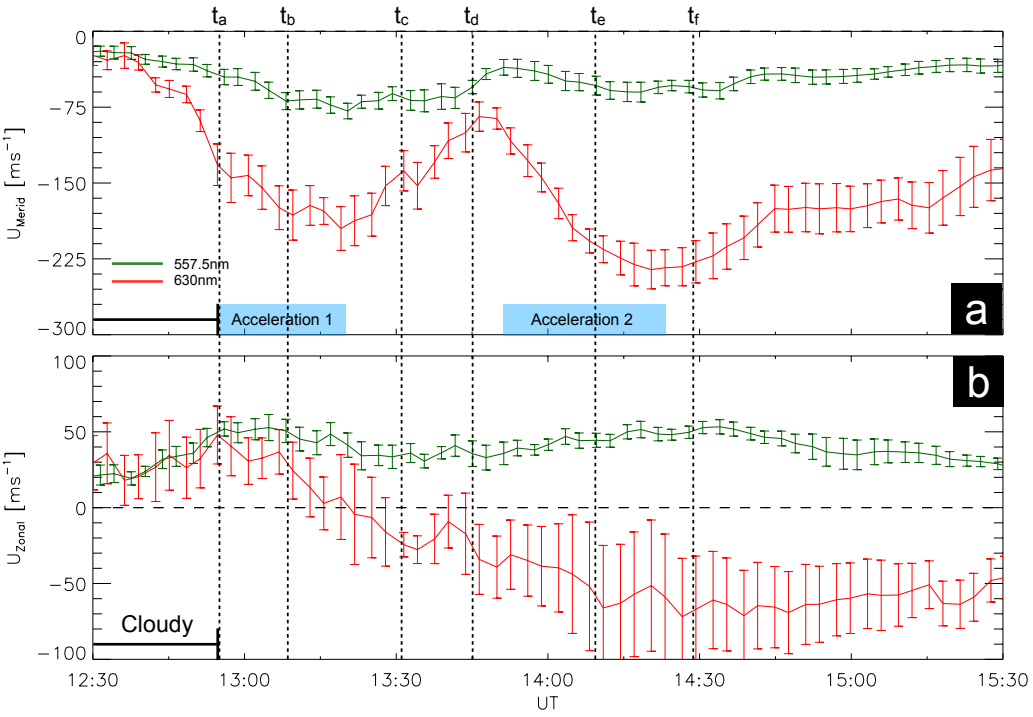

Figure 3. Average (a) meridional (geomagnetic north positive) and (b) zonal (geomagnetic east positive) neutral velocities measured by the Poker Flat SDI for both 557.7 nm (green) and 630 nm (red) emissions. It was cloudy before 12:55 UT, which could have affected the data quality. Error bars are standard deviations, and the two time periods of distinct equatorward acceleration are highlighted for reference. The times denoted by dashed lines t_a through t_f correspond to panels shown in Figures 5 and 6.

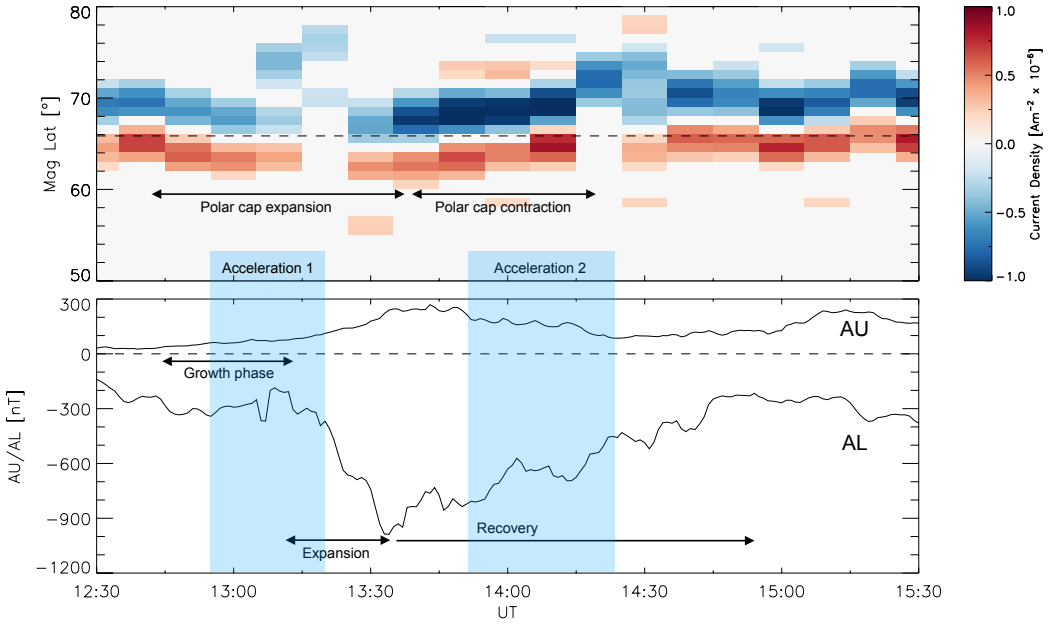

Figure 4. Keogram style FAC data from AMPERE (top) and geomagnetic AU/AL indices (bottom). Presumptive substorm phases have been labelled on the bottom panel, and the periods of equatorward neutral wind acceleration are shaded light blue. The latitude of the Poker Flat SDI has been shown for reference as the horizontal dashed line in the top panel.

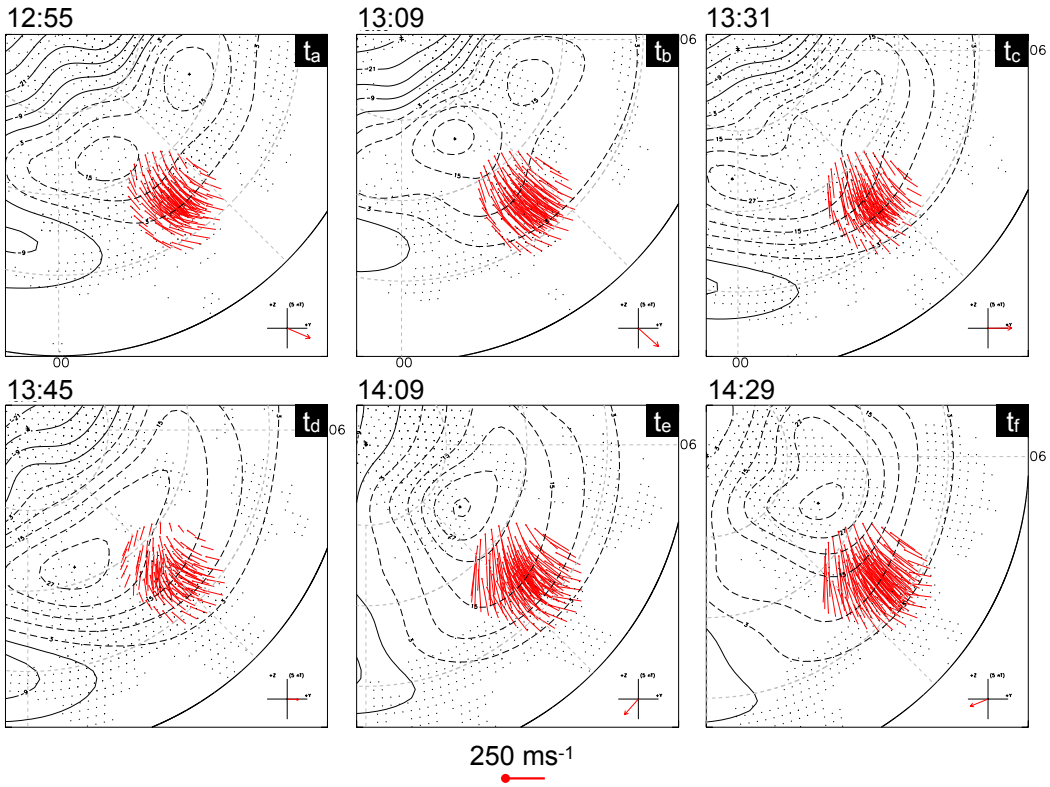

Figure 5. Magnetic latitude - magnetic local time polar plots, centred on Poker Flat SDI FOV, with noon towards the top and dawn to the right. Overlain are the SuperDARN measured electrostatic potential contours (black solid and dashed lines in kV, 6 kV spacing), as well as the F-region neutral winds measured by the Poker Flat SDI. Dots illustrate where SuperDARN radars obtained ionospheric backscatter, and times chosen correspond to before (t_a , t_d), during (t_b , t_e), and after (t_c , t_f) the two acceleration periods. Radial lines separate 3 hours of magnetic local time (numbers shown on outside), and concentric circles separate 10 degrees of geomagnetic latitude. The IMF clock angle is also shown in the bottom right of each panel.

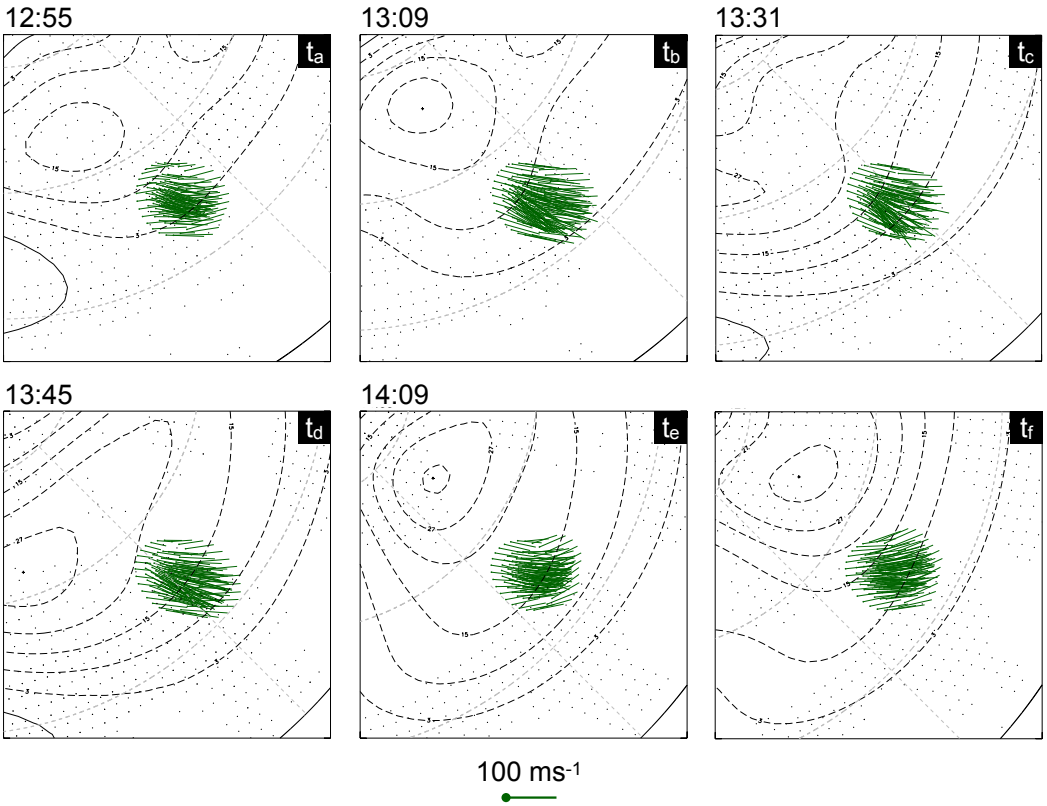

Figure 6. Same as Figure 5, but with the E-region neutral winds and zoomed in closer.

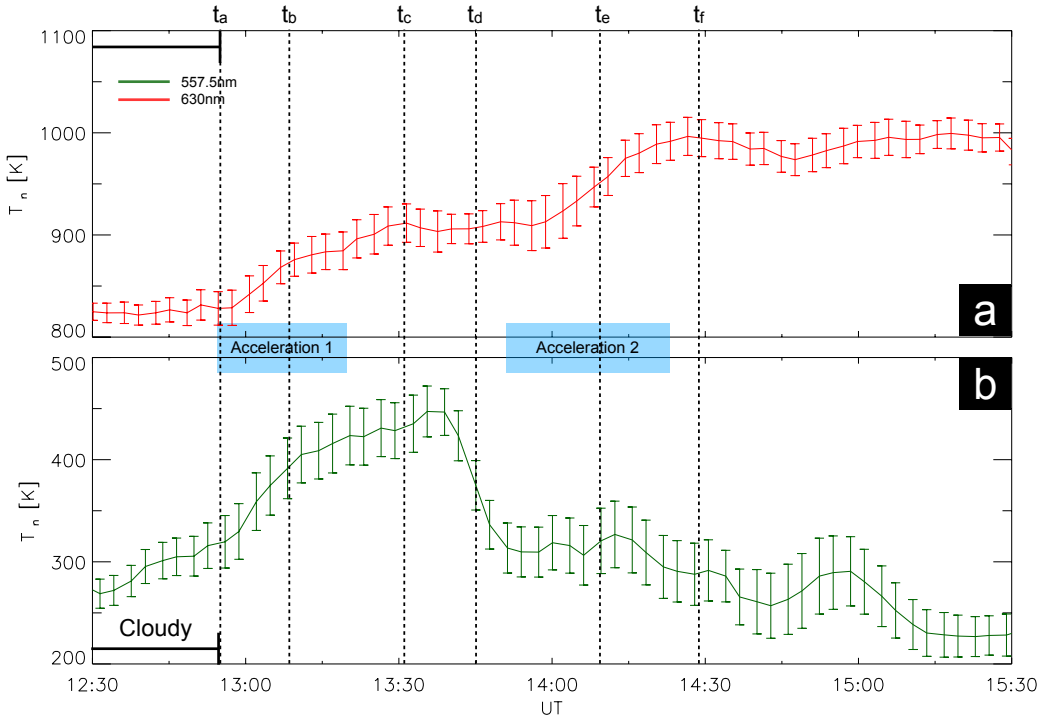

Figure 7. Average neutral temperatures measured by the Poker Flat SDI for both 630 nm (red, a) and 557.7 nm (green, b) emissions. Error bars are standard deviations, and the equatorward accelerations and times from Figure 3 are highlighted and labelled again for reference.